Persistency of ocean swell fields observed from space

Fabrice Collard, Fabrice Ardhuin, Bertrand Chapron

▶ **To cite this version:**

Fabrice Collard, Fabrice Ardhuin, Bertrand Chapron. Persistency of ocean swell fields observed from space. 2008. hal-00346656v2

HAL Id: hal-00346656

https://hal.science/hal-00346656v2

Preprint submitted on 9 Jan 2009 (v2), last revised 23 Feb 2009 (v3)

HAL is a multi-disciplinary open access archive for the deposit and dissemination of scientific research documents, whether they are published or not. The documents may come from teaching and research institutions in France or abroad, or from public or private research centers.

L'archive ouverte pluridisciplinaire **HAL**, est destinée au dépôt et à la diffusion de documents scientifiques de niveau recherche, publiés ou non, émanant des établissements d'enseignement et de recherche français ou étrangers, des laboratoires publics ou privés.

Persistency of ocean swell fields observed from space

Fabrice Collard

Collecte Localisation Satellites, division Radar, Plouzané, France

Fabrice Ardhuin

Service Hydrographique et Océanographique de la Marine, Brest, France

Bertrand Chapron

Laboratoire d'Océanographie Spatiale, Ifremer, Centre de Brest, Plouzané, France

Abstract. Using global satellite Synthetic Aperture Radar (SAR) observations, swell systems are confirmed to travel over very large distances across ocean basins. Satellite observations can provide a global view of swell systems when using a specific "wave mode" sampling. The data are gathered globally and systematically, but the SAR-derived peak wavelength and directional parameters are restricted to the longer swell detected systems for which the SAR-mapping distortion is minimal. Owing to the quality of the retrieved swell parameters, the methodology is shown to provide accurate estimates of the swell arrival times up to 6 days ahead. When reversed, propagation yields well defined swell sources associated with storms. Far away from these sources, and in the absence of dissipation, the swell height should decrease asymptotically like $1/\sqrt{(\alpha \sin \alpha)}$ with α the spherical distance on the Earth surface. In practice, estimated values of H_{ss} can deviate significantly from that asymptote, providing a measure of swell energy dissipation. One of the largest recorded storms provides a striking example in which observations of 15 s period swells are consistent with a constant dissipation rate that corresponds to a 3300 km e-folding scale for the energy. This relatively high dissipation is a significant term in the energy balance of ocean waves at global scales.

1. Introduction

Storms over the ocean produce long surface gravity waves that propagate as swell out of their generation area. In deep water, the wave phase speed C and period T are proportional. As the phase speed of the dominant waves C_p does not exceed 1.2 times the wind speed at 10 m height U_{10} [*Pierson and Moskowitz*, 1964], the longest period waves must be generated by very intense winds. For example, the generation of waves of period T larger than 16 s requires winds with speeds over 18 m s^{-1} blowing over a distance of the order of 1000 km, to produce a significant energy, or yet stronger winds over a shorter fetch [*Munk et al.*, 1963]. Such a large region of high winds is generally associated with a smaller storm center from which the long swells radiate. Away from that core, long period swells have been observed to propagate over very large distances, up to halfway around the globe [*Munk et al.*, 1963], radiating a large amount of momentum and energy across ocean basins. This measurable long-distance propagation is made possible by a limited loss of energy.

The wave field at any time t, latitude ϕ and longitude λ, is described by its its spectral densities G as a function of frequency f and direction θ. In the limit of geometrical optics, this spectral density is radiated at the group speed C_g in the direction of wave propagation, and can be expressed as a function of G at any previous time t_0. Allowing for a spatial decay at a rate μ, the spectral energy balance [e.g. *Munk et al.*, 1963] is

$$G(t,\phi,\lambda,f,\theta) = G\left(t_0,\phi_0,\lambda_0,f,\theta_0\right) \exp\left(\int_{t_0}^{t} -\mu C_g \mathrm{d}t\right) \quad (1)$$

Copyright 2009 by the American Geophysical Union.
0148-0227/09/$9.00

In deep water without current, the initial position ϕ_0, λ_0 and direction θ_0 are given by following the great circle that goes through the point of coordinates ϕ, λ with a direction $-\theta$ over a distance $X = (t - t_0)C_g = (t - t_0)g/(4\pi f)$. This corresponds to a spherical distance $\alpha = X/R$ along the great circle, where R is the Earth radius.

Equation (1) can be used to invert μ from wave measurements. For swell periods shorter than 13 s, *Snodgrass et al.* [1966] have measured an e-folding scale $L_e = 1/\mu = 5000$ km (this number corresponds to a 0.1 dB/degree attenuation in their analysis). For larger periods, *Snodgrass et al.* [1966] could only conclude that L_e is larger, possibly infinite. In the past 40 years, little progress has been made on these conclusions [*WISE Group*, 2007]. Yet this question if of high practical importance, either for wave forecasting [e.g. *Rascle et al.*, 2008] or other geophysical investigations regarding air-sea fluxes or microseismic noise [e.g. *Grachev and Fairall*, 2001; *Kedar et al.*, 2008].

A theoretical upper bound for L_e is given by the viscous theory [*Dore*, 1978]. In that theory, the largest shears are found right above the water surface, and the air viscosity dominates the dissipation of swells, giving, in deep water,

$$L_{e,\max} = \frac{\rho_w g^2}{4\rho_a \sigma^3 \sqrt{2\nu_a \sigma}}, \quad (2)$$

where ν_a is the air viscosity, $\sigma = 2\pi/T$. For $T = 13$ s this gives $L_{e,\max} = 45000$ km, which means that over a realistic propagation distance of 10000 km the energy of 13 s swells is only reduced by 25%.

Swells are thus expected to be very coherent over distances that are only limited by the size of ocean basins. The analysis of swells at this global scale should provide insights into their dynamics, including propagation and dissipation, but also into the structure of the generating areas, in a way similar to the use of the cosmic microwave background for

the analysis of the early universe. The present paper provides two important intermediate steps toward that goal. First, we demonstrate in section 2 how sparse data from a single space-borne synthetic aperture radar can be combined dynamically to provide a consistent picture of swell fields. This internal consistency reveals the quality of the SAR-derived dataset which we further verify quantitatively with buoy data. In section 3, we discuss and derive the asymptotic far-field swell energy evolution. Numerical investigations are performed to check the validity of the asymptotic solutions. This result provides a tool to interpret measured swell heights in terms of propagation and dissipation. This method is illustrated with one example that corresponds to a strong swell dissipation. Conclusions follow in section 4.

2. Space-time consistency of space-borne swell observations

Investigations by *Holt et al.* [1998] and *Heimbach and Hasselmann* [2000] have shown that space-borne synthetic aperture radar (SAR) data can be used to image the same swell field over 3 to 10 days as it propagates along the ocean surface. These preliminary studies have shown that the combination of SAR data at different places and times yields a position of the generating storm, and predictions for the arrival time of swells with different periods and directions. *Heimbach and Hasselmann* [2000] have further pointed to shortcomings in the wind forcing for a given Southern Ocean storm, based on systematic biases in wind-forced wave model results compared to SAR observations. Unfortunately, the systematic analysis of such data has been very limited, and generally confined to data assimilation in wave forecasting models [e.g. Hasselmann *et al.* 1997; Breivik *et al.* 1998; Aouf *et al.* 2006]. This narrow use of SAR data is due to two essential difficulties.

First, a SAR image is not a picture of the ocean surface and the relationship between the spectrum of the SAR image and that of the ocean surface elevation is nonlinear and fairly complex [e.g. *Krogstad*, 1992]. Sophisticated methods have been developed in order to estimate the surface elevation spectrum [e.g. *Hasselmann et al.*, 1996; *Schulz-Stellenfleth et al.*, 2005]. These methods had to be implemented by the user of the data, and generally required some *a priori* first guess of the wave field provided by a numerical model. For longer wave systems, the imaging mechanisms are essentially quasi-linear, making possible a simpler methodology used by the European Space Agency (ESA) to generate a level 2 (L2) product. The method is fully described by *Chapron et al.* [2001]. It uses no outside wave information, and builds on the use of complex SAR data developed by *Engen and Johnsen* [1995] to remove the 180° directional ambiguity in wave propagation direction. The quality of the L2 data has been repeatedly analyzed [e.g. *Johnsen and Collard*, 2004; *Collard et al.*, 2005]. Because long ocean swells have large wavelengths and smaller steepnesses, the L2 products corresponding to this spectral range have higher relative quality, confirming that the imaging mechanism is well described under the quasi-linear assumption.

All SAR data used here are such L2 products, provided by ESA and obtained with the L2 processor version operational since November 2007, and described by *Johnsen and Collard* [2004]. The data for times before that date were reprocessed with this same processor. In previous real-time data, frequent low wavenumber artefacts were caused by insufficient filtering of non-wave signatures in the radar images. This filtering is necessary to remove the contributions of atmospheric patterns or other surface phenomena like ships, slicks, sea ice, or islands, with spectral signatures that can overlap the swell spectra. The L2 product contains directional wave spectra with a resolution of 10° in directions and an exponential discretization in wavenumbers spanning wavelengths of 30 to 800 m with 24 exponentially spaced wavenumbers, corresponding to wave periods with a 7% increment from one to the next.

As mentioned above, long crested swells are very weakly distorted by the SAR imaging mechanism. A constructive phenomenon further participates to improve image contrasts [*Alpers and Rufenach*, 1981]. Consequently, for a simple use of SAR data, spectral partitioning analysis should be performed to retrieve the height H_{ss}, peak period T_p and peak directions θ_p not affected by the azimuth cut-off effect due to the wave orbital velocity randomness [*Kerbaol et al.*, 1998].

The second practical problem, is that the data obtained from an orbiting platform are sparse and with a sampling that makes a direct analysis difficult. Hereafter, we show that the space-time consistency of the swell field can be used to fill in the gaps in the observations and produce continuous observations of swell periods and directions in space and time.

2.1. Virtual buoys

For each wave spectrum observed in the world ocean, swell partitions are extracted providing estimations of H_{ss}, T_p, and θ_p. In practice, the L2 spectra are first smoothed over 3 direction bins (30° sectors) and 3 wavenumber bins. The peaks are then detected and the energy associated to each peak is obtained by the usual inverted water-catchment procedure [*Gerling*, 1992]. The swell peak period is defined as the energy-weighted average around ±22% of the frequency with the maximum energy. Given these SAR-derived estimates, linear dispersion relationship and the principle of geometrical optics can then be exploited to predict arrival times and locations of the swell. Likewise the peak direction θ_p is defined as the energy-weighter direction within 30° of the peak direction.

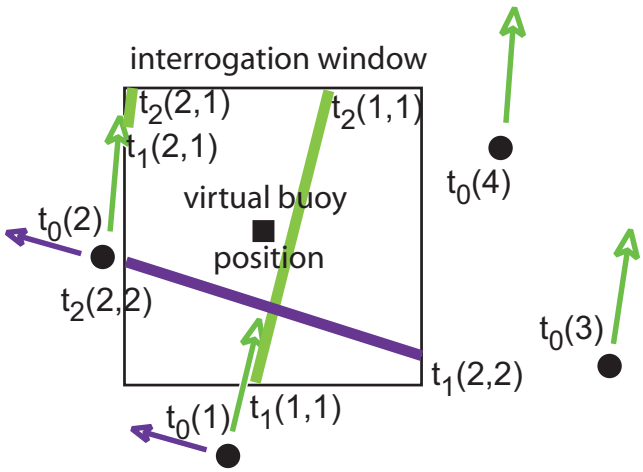

Figure 1. Schematic definition of a virtual buoy. Any SAR observation i is available at a time $t_0(i)$ on the black dots. All swell partitions (i, j) (here indicated by the arrows) are propagated and may cross the interrogation window from time $t_1(i, j)$ to $t_2(i, j)$.

In order to obtain swell conditions at the location of a "virtual buoy", we define an interrogation window covering 2 by 2 degrees in latitude and longitude. According to the SAR-derived peak parameters, swell partitions from the entire ocean basin are propagated, both forward and backward, along great circles in space and time. These theoretical trajectories are followed with a constant group speed

$gT_p/(4\pi)$, starting off in direction θ_p from the observation point. From any observation time t_0, these great circles may cut through the interrogation window from times t_1 to t_2 (thick solid lines in figure 1, with different colors for different partitions). As the maximum value of $|t_2 - t_0|$ and $|t_1 - t_0|$ is increased from 6 hours to 6 days, the time-evolution of the peak frequencies and peak directions at the virtual buoys gradually reveals similar ridges to the one observed in real buoy measurements (figure 2).

In fig. 2b-d, each horizontal colored segment corresponds to one swell partition that crosses the spatial window between times t_1 and t_2. Some segments are very short, corresponding to trajectories that barely cut one corner of the window.

Clearly the SAR detects the directions of the most energetic part of the wave spectrum measured by the buoys (fig. 2a). At frequencies above 0.1Hz, the virtual buoy patterns appear rather noisy. Shorter scales are not so coherently observed. Besides, these shorter components are often observed as part of the wind sea for which the propagation with a single group speed and direction is not a good approximation. Also, propagated high frequency swells, such as the 0.12 Hz waves coming from direction 200 on July 10, do not show up in the real buoy record. This is possibly the result of a relatively high dissipation rate for these swells.

For frequencies below 0.08 Hz, the virtual buoy shows ridge-like structures similar to those observed *in situ* due to the dispersive arrivals of swells from remote storms [e.g. *Munk et al.*, 1963; *Gjevik et al.*, 1988]. Even the faintest events are well detected, such as the 0.06 Hz arrival on 23 July, even though that 15 s swell of 0.5 m is dwarfed by a another 0.8 m 12 s swell and a 8 s 2 m wind sea. Swell detection with the virtual buoy reaches its limits when the swell height is very low, such as on 3 July with a 20 s 0.3 m swell well detected by the buoy (the green-orange ridge at 0.05 Hz). Because we use a single trajectory emanating from one observed swell partition the relatively small interrogation window can easily be missed after 10000 km of propagation. An extension of the present technique could use neighboring directions to take into account the directional spread of the sea state. Other errors can also be attributed to the processing technique. In particular, a maximum value is defined for the transfer function used to obtain the wave spectrum from the SAR image [*Johnsen and Collard*, 2004]. Although this is designed to prevent the amplification of measurement noise, such long swells have very small slopes and it is likely that they would not be well transformed in the wave spectrum due to this threshold in the processing.

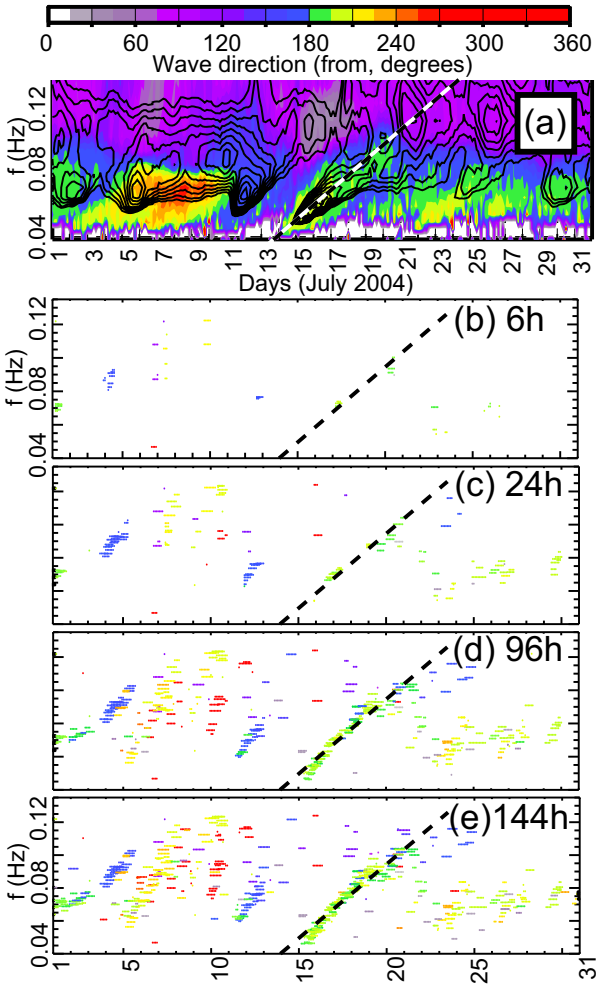

Figure 2. (a) Energy and mean direction spectrum measured in situ by the Christmas Island buoy (WMO number 51028): contours, equally spaced from 0.1 to 1.4, indicate the natural logarithm of the spectral energy density $F(f)$. Colors indicate the mean arrival direction at each frequency. (b) to (e) Peak direction (colors) as a function of time and peak frequency for swell partitions at a SAR virtual buoy located around the Christmas Island buoy (WMO number 51028). The maximum propagation time to produce the virtual buoy data is increased from 6 hours (b) to 6 days (e). The sloping straight line fitted to the observed SAR ridge from July 16 at 0.05 Hz to July 21 at 0.105 Hz is the same as line in (a) that corresponds to the buoy observation. This delayed arrival would correspond to a point source at 6100 km from Christmas Island.

When propagated for 6 days, without any other information than the peak frequency and direction at the time of observations, the waves are remarkably coherent with the latest local observations. For the southern swells arriving at Christmas Island between July 16 and 21 (figure 2), the difference in arrival times given by the virtual and real buoys is typically less than 12 h. This is less than 10% of the maximum time between the SAR observation and the virtual buoy record. This implies that the accuracy of the peak period estimate for each SAR partition must also be less than 10%. The consistency of the arrival directions along the

ridges also suggests that the root mean square (RMS) error in peak direction estimates must be close to 20°, comparable to the 22° RMS difference between mean wave directions obtained from SAR wave mode and a numerical wave model for waves with periods longer than 12 s [*Johnsen and Collard*, 2004].

2.2. Storm source identification and "fireworks"

Along the estimated trajectories, virtual observations can further be produced in a similar fashion. The animation of these propagated swells confirms the very well organized nature of storm swells crossing large ocean basins. From the relatively sparse and track-based initial satellite observation sampling, the swell persistency can then be used to capture "fireworks" patterns exploding from the few intense storms that occur over a period of several days (see figure 3 and auxiliary animation).

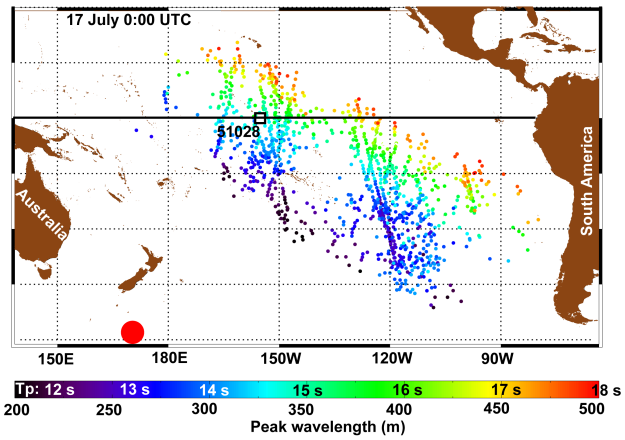

Figure 3. Snapshot of the "fireworks" animation on July 17 2004 at 0:00 UTC. Each of the 1071 colored dots represent one observed swell partition, within 6 days of its observation, displaced along a great circle with the group speed corresponding to the detected peak period in the direction of the detected peak direction. Only swells with tracks that passes within 1000 km of the storm center (red disk) have been retained.

In large ocean basins where swells are likely to be imaged several times by the same satellite, these fireworks can be used to estimate the time of arrival of swells from any given storm [e.g. *Holt et al.*, 1998]. For this reason, these animations have been produced routinely every day since August 2007, for the Pacific, Indian, and Atlantic oceans (see in http://www.boost-technologies.com/esa/images/, e.g. `nrt_pac.gif` for the Pacific Ocean).

Using backward trajectories, the location and date of swell sources can further be defined as the spatial and temporal center of the convergence area and time of the trajectories. These positions have been verified to correspond to high wind conditions observed by scatterometers and reproduced by ECMWF wind analyses. We consider these storms to be the source of all the swell partitions that produce trajectories that pass within 12 hours and 2000 km of their center. This processing, similar to the one performed by *Heimbach and Hasselmann* [2000], provides a global view of swell fields in both space and time, extending the coverage of similar techniques based on buoy data [*Hanson and Phillips*, 2001]. In figure 4, a swell covers one Earth quadrant away from the storm, with a large detection gap that extends from the Southern Pacific to California. This blank area is the

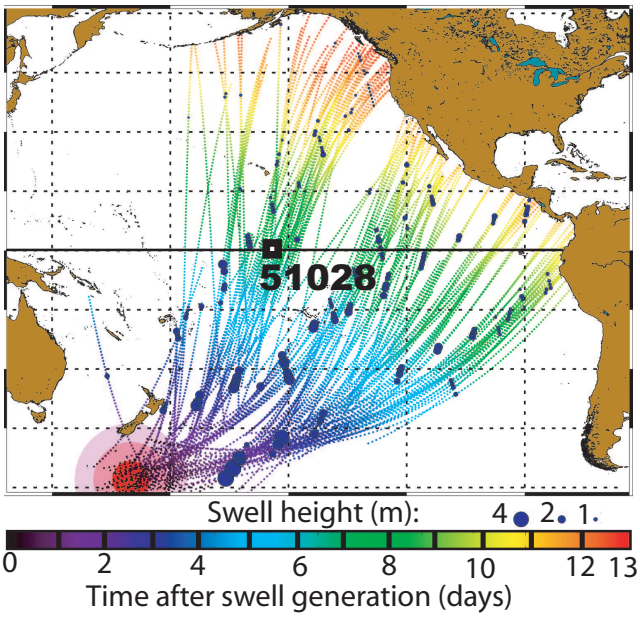

Figure 4. Finding the source storm. All swells with a 17 ± 0.5 s period that were identified in 13 days of ENVISAT synthetic aperture radar data over the Pacific, are re-focussed from their location of observation (filled dots) following their direction of arrival at the theoretical group speed for 17 s waves. This focussing reveals a single swell generation event, well defined in space and time (pink to red disks). The back-tracking trajectories are color-dated from black (July 9 2004 18:00 UTC) to red (July 22 2004 18:00 UTC).

long shadow cast by French Polynesia where wave energy is dissipated in the surf [e.g. *Munk et al.*, 1963]. Observations were restricted to swell partitions with periods close to 17 s, but the full dataset typically covers swells with periods of 12 to 18 s, as shown in figure 3.

2.3. Quantitative validation of T_p and H_{ss}

The apparent self-consistency of both the virtual buoy plot (figure 2.d) and the fireworks animations, are the result of the spatial coherence of the swell fields, which was expected from the in situ measurements of *Darbyshire* [1958]; *Munk et al.* [1963]; *Snodgrass et al.* [1966]. Yet, these plots could not exhibit such coherent patterns without a good accuracy of the SAR-derived peak periods and directions, used in the propagation methodology.

A classical analysis of SAR estimation errors is provided by a direct comparison of swell parameters, estimated from level 2 products, with buoy measurements at nearly the same place and time [*Holt et al.*, 1998; *Johnsen and Collard*, 2004].

Previous validations were presented for the total wave height H_s [*Collard et al.*, 2005] or a truncated wave height H_{s12} defined by chopping the spectrum at a fixed frequency cut-off of 1/12 Hz. For that parameter, *Johnsen and Collard* [2004] found a root mean square (RMS) difference of 0.5 m, when comparing SAR against buoy data, including a bias of 0.2 m. In the present study, we use H_{ss} values obtained from both SAR and buoy spectra. A preliminary validation of H_{ss} was performed by *Collard et al.* [2006], using L2 processing applied to 4 by 4 km tiles from narrow swath images exactly located at buoy positions. That study found a 0.37 m r.m.s. error. This smaller error was obtained in spite of a 4 times smaller image size, suggesting that a

Table 1. Error statistics for swell partitions heights and peak periods derived from SAR wave mode data (after bias correction) against buoy-derived data, for subsets A, B and C of the co-located database. Subset A contains 2399 observations. Subset B is restricted to $U_{10SAR} \leq$ 8m/s and contains 1936 observations. Subset C is further restricted to SAR-buoy distances less than 100 km, and contains only 460 observations. RMSE stands for root mean square difference, while the NRMSE is the RMSE normalized by the root mean square observed value. The scatter index (S.I.) is equivalent to the NRMSE computed after bias removal. Finally, r is Pearson's linear correlation coefficient.

	H_{ss}	T_{ps}
subset A, bias	0.00 m	0.27 s
subset A, RMSE	0.38 m	1.14
subset A, S.I.	24.0%	7.9%
subset A, NRMSE	24.0%	8.2%
subset A, r	0.91	0.61
subset B, bias	0.00 m	0.24 s
subset B, RMSE	0.35 m	1.11 s
subset B, S.I.	23.5%	7.8%
subset B, NRMSE	23.5%	8.0%
subset B, r	0.92	0.62
subset C, bias	0.02 m	0.32 s
subset C, RMSE	0.29 m	1.07 s
subset C, S.I.	22.4%	7.3%
subset C, NRMSE	22.5%	7.7%
subset C, r	0.92	0.64

significant part of the "errors" in SAR validation studies are due to the distance between SAR and buoy observations.

The swell height validation has been repeated here, using all buoy data from 2004 to 2008, located within 200 km and 1 hour of the SAR observation. These co-located data are made publically available as part of the XCOL project on the CERSAT ftp server managed by Ifremer. Because we wished to avoid differences due to coastal sheltering and shallow water effects, we restricted our choice of buoys to distances from the coast and the 100 m depth contour larger than 100 km. As a result, most selected buoys are not directional, and we use partitions in frequency only. For the present validation, differently from other section of this paper, we thus define a swell partition as the region between two minima of the frequency spectrum. The corresponding energy E_s gives the swell height $H_{ss} = 4\sqrt{E_s}$. The buoy swell height is then defined from the energy contained within the frequency band of the SAR partition. The peak period is then estimated as the period where the buoy spectrum is maximum. The database includes 15628 swell partitions observed by the SAR, with matched buoy swell partitions.

Many of these observations correspond to relatively short swells, for which the waves are poorly imaged. We have thus defined a subset of the database by imposing the following conditions. First the image normalized variance, linked to the contrast intensity and homogeneity, should be in the range 1.05 to 1.5, which limits the dataset to 6651 observations. This removes SAR data with non-wave features (slicks, ships ...) that would otherwise contaminate the wave spectra. Second, both the SAR and buoy peak periods are restricted to the 12 to 18 s range, which reduces the dataset to 4136 observations, and removes most of the problems related to the azimuthal cut-off. Third and last, the SAR-derived wind speed U_{10SAR} is limited to range from 3 to 9 m s^{-1} in order to remove low winds with poorly contrasted SAR images and high winds which may still cause some important azimuthal cut-off and contamination of swell spectra by wind sea spectra. This gives subset A, with 2399 observations.

For subset A, H_{ss} has a bias of 0.24 m and the standard deviation of the errors is 0.4 m. The bias is found to be primarily a function of the swell height and wind speed, increasing with height and decreasing with wind speed. Variations in standard deviation are dominated by the swell height and peak period, with the most accurate estimations for intermediate periods of 14 to 17 s.

We thus corrected the SAR-derived swell heights by subtracting a bias model given by

$$b_h = 0.11 + 0.1H_{ss} - 0.1\max\{0, U_{10SAR} - 7\} \qquad (3)$$

where H_{ss} is in meters and the wind speed U_{10SAR} is in m s^{-1}. The resulting heights are compared to buoy measurements in figure 5

When the maximum wind is reduced to 8 m s^{-1}, giving subset B, the differences between SAR and buoy data is reduced, with further reductions when the maximum distance between SAR and buoy data is reduced from 200 to 100 km to give subset C (table 1).

In subset C the data was clustered according to wind speed and wave height. For all of these clusters, the standard deviation of H_{ss} estimates is reduced to less than

$$\sigma_h = 0.10 + \min\{0.25H_{ss}, 0.8\} \qquad (4)$$

where σ_h and H_{ss} are in meters.

3. Far-field swell energy

All these illustrations of forward-backward ray tracing indicate the potential to use a simple Geometrical Optics (GO) strategy. The next goal is then to determine the strength

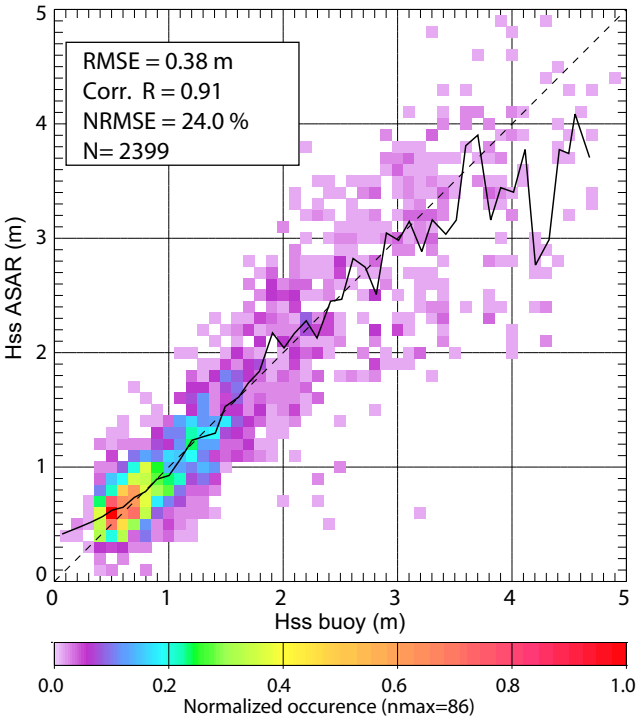

Figure 5. ASAR-derived swell partition heights versus buoy swell partition heights after bias correction using eq. (3), for subset A. The solid line joins the median values from SAR observations in each 0.1 m class of buoy-measured height.

of the far-field radiated swell energy. This requires the definition of a swell source, and an estimation of the swell energy dissipation scale. For this we define the time t_0 as an initial condition after which there is no significant wave generation or non-linear evolution, for frequencies less than $f_{\max}$. Namely, at t_0 all the wave components with smaller frequencies have already been generated, so that the radiation of these waves is essentially fossil and fully governed by geometrical optics. The possible effects of diffraction and scattering are discussed by *Munk et al.* [1963], and, together with dissipation, will cause deviations from the G.O. model outlined below.

In reality, swells evolve over the course of their propagation as the result of their interactions with the local winds, mutual wave-wave interactions, interactions with other wave systems, including the local wind sea. Swells also evolve according to interactions with other oceanic motions that affect the upper ocean, namely surface currents, internal waves and turbulence. Depth and island scattering effects must also carefully be taken into account [*Snodgrass et al.*, 1966; *WISE Group*, 2007]. Besides these different mechanisms, dispersion and angular spreading effects are certainly the first leading order phenomena to take into account for the major part of the decrease in the height of the swell systems. Indeed, as the long swell systems will be characterized by relatively small steepness parameters, nonlinear mutual wave-wave interactions do not appear to be important in scattering surface wave energy more than a few storm radius distances outside an active generating area. Furthermore, the level of turbulence in the ocean does not appear to significantly affect the waves, and the conversion of surface wave energy into internal gravity wave energy by wave-wave interactions does not seem to be a leading order sink term for the energy balance of surface gravity waves. Finally, for the very long trans-ocean fast propagating swell components, surface current bending effects, proportional to the ratio between vertical current vorticity and the group velocity, may also be considered as residual effects. Away from island obstructions, the ratio between the angular width along the great-circle observatory points at very large distances from the generating area, and the mean spread in the generating area is approximately proportional to $1/\sin\alpha$ with α the spherical distance from the storm. center The change in spectral density F defined by

$$F(t,\phi,\lambda,f) = \int_0^{2\pi} G(t,\phi,\lambda,f,\theta)d\theta \qquad (5)$$

follows the spatial expansion (close to the source) and contraction (as waves approach the antipodes for $\alpha > \pi/2$) of the energy front. This transversal dispersion is associated to a narrowing of the directional spectrum G, for $\alpha < \pi/2$, and a broadening for larger distances.

This approximation applies to large distances, and relatively small source regions. Closer to the source, the approximation does not hold. Swell amplitudes radiating from large extended sources will decrease more slowly than swell amplitudes emanating from compact sources.

Moreover, we can represent swell waves as a linear superposition of harmonic waves in narrow spectral band. Quite naturally, through the method of stationary phase, the group velocity is defined and the slowly-varying wave envelope is found to decay. This decay is inversely proportional to the square-root of the distance (figure 6). Accordingly, far away from the generating sources, and in the absence of dissipation, the swell energy

$$E_s(t,\phi,\lambda) = \int_0^{\infty} F(t,\phi,\lambda,f)\mathrm{d}f. \qquad (6)$$

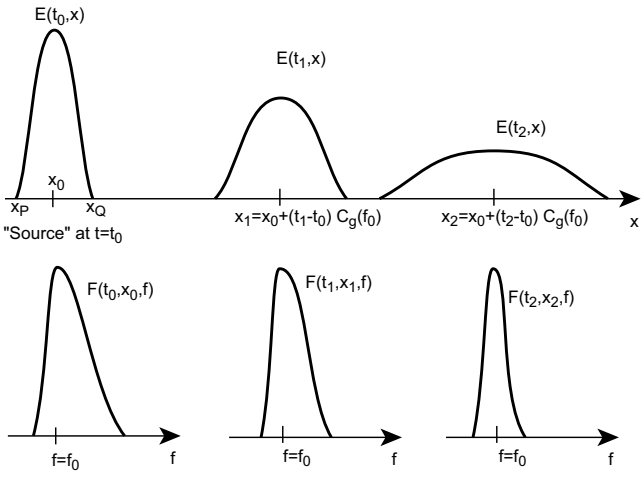

Figure 6. Dispersion of linear waves in one dimension. At any given time the spectrum is given by a propagation of the spectra at $t = t_0$. Taking $x_1 = x_0 + (t_1 - t_0)C_g(f_p)$ the spectral density at f_p is the same as for time t_0, but the spectrum is narrower which gives a smaller elevation variance, $E(t_1, x_1) < E(t_0, x_0)$.

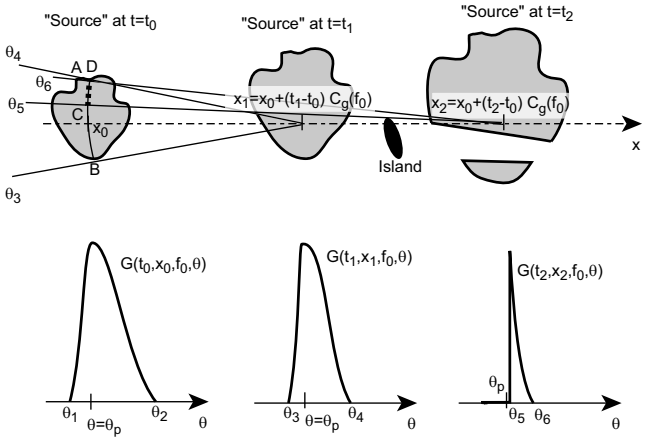

Figure 7. Dispersion of linear waves in two dimension, represented here on a flat surface for simplicity. The variable y has been dropped as the spectra shown here are all at $y = 0$. We call "source" the region of the ocean where waves with frequencies smaller than $f_{\min}$ can be found. As time goes by, the source expands in space due to both frequency dispersion (like in 1D), and geometrical dispersion. The wave energy with frequency f_0 that will be observed at point x_1 (respectively x_2) at time t_1 (respectively t_2) is, at time t_0, along the thin arc circle AB (respectively the thick dotted arc circle CD). Due to the small island between x_1 and x_2, the energy that would have been recorded at x_2, if the island were not present, is actually dissipated on the shore of the island. As a result the local energy density $E(x_2)$ is reduced. At frequency f_0, contributions to $E(x_2)$ only come from angles θ_5 to θ_6. The directional spectra (bottom) are thus affected by the blocking effect of islands, and the directional narrowing as one goes further from x_0 (on the Earth this narrowing reverses after 10000 km of propagation, due to the sphericity).

should decrease asymptotically like $1/(\alpha \sin\alpha)$ when following a wave group.

3.1. The *Snodgrass et al.* [1966] method

Using measurements with a limited or no directional resolution, *Snodgrass et al.* [1966] assumed that wave propagation was completely blocked by waters shallower than 60 fathoms (approximately 110 m), and that diffraction could be neglected. For example, in figure 7, the island would be represented by the 60 fathom depth contour. These authors then estimated a loss of swell energy from the deviation of the ratio of directionally-integrated spectra, e.g. $F(x_2, f_0)/F(x_1, f_0)$, compared to what is expected from the lateral dispersion effect, taking into account islands. Currents, shallow water areas and diffraction effects around islands are neglected here. These effects are discussed by *Snodgrass et al.* [1966].

Rigorously, their method is inexact because the recording stations x_1 and x_2 measure wave groups that had neither exactly same propagation directions nor the same position when they were near x_0. Yet, because the wave field in the neighborhood of x_0 is the superposition of many independent wave trains, one can *assume* that the spectral density F is a smooth function of the direction. Then we may say that over the intervals θ_3 to θ_4 or θ_5 to θ_6, G does not change so much, i.e. in figure 7, $G(t_0, \phi_D, \lambda_D, f, \theta_6) \simeq G(t_0, \phi_D, \lambda_D, f, \theta_5)$. On the sphere the application of eqs. (1) and (5) yields

$$F(t,\phi,\lambda,f_0) = \frac{1}{\sin\alpha}\int_C^D G(t_0,\phi,\lambda,f_0,\theta_0)\frac{\mathrm{d}s}{R}\left[1+O\left(\frac{1}{\sin\alpha}\right)\right], \tag{7}$$

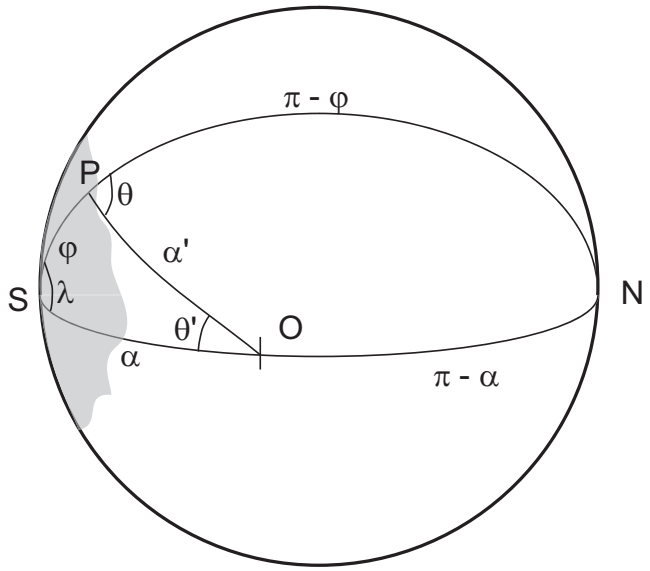

Figure 8. Geometry of the generating storm (shaded area) and observation conditions. Any point P of colatitude φ and longitude λ inside of the storm, generates waves that are observed at point O. At time t the observed waves that come from P have a well defined frequency given by eq. (9), function of the spherical distance α' between P and O, and a well defined direction θ at P, relative to the North, which gives a direction $\pi - \theta'$ at O. In the triangle OPS the angles λ, θ' and $\pi - \theta$ are related to the distances α',φ and α by the usual spherical trigonometry relationships, e.g. eq. (11).

where the integral is performed over the line segment joining C to D. The error relative to the asymptote is the sum of two terms. One is proportional to the spatial gradient of F, due to the change from the arc circle to the segment, and the other corresponds to the relative variation of G with θ over the range θ_5 to θ_6, which is small in the far field, provided that the directional spectrum is smooth enough.

Under these two smoothness assumptions, and for large $\sin(\alpha)$, the ratios of spectral densities F at x_1 and x_2, as used by *Snodgrass et al.* [1966], can indeed be used to diagnose the conservation of swell energy. This does not apply if x_1 is in the vicinity of the storm or its antipode, where the observed arrival direction span a large range.

In practice, this method can be very sensitive to the correct estimation of the island shadowing. For that reason, the measurement route chosen by *Snodgrass et al.* [1966] was far from ideal. Because they needed land to install most recording stations for the wave measurements, they used an almost north-south great circle that extends from the south of New-Zealand (Cape Palisader) to Alaska (Yakutat), a route peppered with islands in its southern part, and partially blocked by the Hawaiian chain in its northern part. Also, storms typically refuse to line up with any measurement array. Their pre-defined great circle, although designed to follow a typical Southern winter swell propagation path, always deviated by some extent form the actual track followed by the most energetic swells they recorded. For the Indian ocean storms, this difficulty was reduced by the relatively narrow range of angles that allows propagation from the Indian to the Pacific ocean.

3.2. A method using global swell heights

Now using an instrument with a global coverage, we can carefully avoid both problems by choosing propagation paths far away from the smallest island, and by exploiting only observations well aligned with the storms. However, due to the limited spectral resolution inherent to the SAR wave mode image size and processing, we cannot use the spectral distribution G or F of the energy, and can only use the energy E_s integrated over a swell partition.

For simplicity, and without loss of generality, we take the source storm centered at time $t_0 = 0$ on the pole S defined by a colatitude $\varphi = \phi - \pi/2 = 0$, so that the distance from the storm center is $r = R\varphi$. We consider the swell energy E_s observed at a position defined by the spherical distance α and we take the reference meridian to be in the direction of the observation point (figure 8).

We will later assume that the source area is relatively small with a size $R\Delta_\alpha$, where Δ_α is the maximum value taken by φ (figure 8). In all the following derivations, we have chosen a fixed frequency f_0 and we follow a wave group of that frequency. The time of observation t is thus related to α by $t = R\alpha/Cg(f_0)$, so that the variable t will be omitted.

E_s is an integral of the local spectrum G over both frequencies f and arrival directions θ,

$$E_s(\alpha) = \int_0^{2\pi}\int_0^{\infty} G\left(t,\phi',\lambda',f,\theta'\right)\mathrm{d}f\mathrm{d}\theta'. \tag{8}$$

Using eq. (1) this local integral, can also be written as an integral over the entire source area Ω. The spherical distance between any point $P(\varphi,\lambda)$ in the source region and the observation point $O(\alpha, 0)$ is α'. The observed frequency that is due to this source point is

$$f = gt/(4\pi R\alpha') = f_0\frac{\alpha}{\alpha'}. \tag{9}$$

We may replace f by α' in eq. (8),

$$E_s(\alpha) = \frac{f_0}{\alpha}\int_0^{2\pi}\int \frac{\alpha^2 G\left(t_0,\phi,\lambda,f,\theta\right)}{\alpha'^2}\mathrm{d}\theta'\mathrm{d}\alpha'. \tag{10}$$

For a circular uniform storm of radius r with isotropic spectra, as used in figure 9, $E_s(\alpha)$ is given by the integral over α' weighted by the directional width of the spectrum $\Delta\theta'$. That width is given by the spherical trigonometry relationship

$$\Delta\theta' = 2\theta'_{\max} = 2\arccos\left[\frac{\cos\varphi_{\max} - \cos\alpha\cos\alpha'}{\sin\alpha\sin\alpha'}\right], \quad (11)$$

with $\varphi_{\max} = r/R$.

For general spectral distribution, we may transform the integration variables (α', θ') which are the colatitude and longitude coordinates on the sphere with a pole at the observation point, to coordinates (φ, λ) with a pole in the storm center. The transformation Jacobian is simply given by the equality of the elementary area on the unit radius sphere $dA = \sin\varphi \mathrm{d}\phi\mathrm{d}\lambda = |\cos\phi|\,\mathrm{d}\phi\mathrm{d}\lambda = \sin\alpha'\mathrm{d}\alpha'\mathrm{d}\theta'$. We thus have

$$E_s(\alpha) = \frac{f_0}{\alpha\sin\alpha}\int_\Omega \frac{\alpha^2\sin\alpha}{\alpha'^2\sin\alpha'} G\left(t_0,\phi,\lambda,f,\theta\right)|\cos\phi|\,\mathrm{d}\phi \quad (12)$$

$$= \frac{f_0}{\alpha\sin\alpha}\left\{\int_\Omega G\left(t_0,\phi,\lambda,f_0,\theta_0\right)dA \times\left[1+O\left(\frac{\Delta_\alpha}{\alpha}\right)\right] + \int_\Omega \left[G\left(t_0,\phi,\lambda,f,\theta\right) - G\left(t_0,\phi,\lambda,f_0,\theta\right)\right]\mathrm{d}A + \int_\Omega \left[G\left(t_0,\phi,\lambda,f_0,\theta\right) - G\left(t_0,\phi,\lambda,f_0,\theta_0\right)\right]\mathrm{d}\phi\right\}. \quad (13)$$

where θ is the direction of the great circle at the generation point that goes through that point and the observation point. θ is thus a function of ϕ, λ, α and θ_0. Δ_α is maximum value of $|\alpha' - \alpha|$, i.e. the radius of the source region divided by the Earth radius.

For continuous spectra, the second integral on the right hand side of eq. (8) goes to zero as α goes to infinity (which, on the sphere is limited by π) since the part of the source spectra that contribute to the observations shrink to a smaller and smaller neighborhood around f_0 and θ_0. The observed frequencies f are limited by

$$|f - f_0| \le \frac{\Delta_\alpha}{\alpha} \quad (14)$$

This is enough to guarantee that this second integral also contributes a deviation ε_2 from the asymptote, limited by

$$\varepsilon_2 \le A\frac{\Delta_\alpha}{\alpha}\max\left\{\frac{\partial G}{\partial f}\right\} \quad (15)$$

where the maximum is taken over all the contributing components.

Similarly, the outgoing directions θ received at the observation point are also limited to a narrow window as α increases, giving another deviation term ε_3. Using the sine formula in the triangle OPN, $\sin\theta/\sin(\pi-\alpha) = \sin\lambda/\sin\alpha'$. Thus, in the far field of the storm and its antipode, θ is close to $\theta_0 = \lambda$. Thus $\sin\theta - \sin\theta_0 = \sin\lambda\left(\sin\alpha - \sin\alpha'\right)/\sin\alpha'$, which is less than $\Delta_\alpha/\sin\alpha'$, and therefore $|\theta - \theta_0|$ is less than $\arcsin\left(\Delta_\alpha/\sin\alpha'\right)$. If one does not get too close to the storm or its antipode (say, $\Delta_\alpha < \alpha < \pi - 2\Delta_\alpha$) then we can give an upper bound of $1/\sin\alpha'$ as a function of α and obtain

$$\varepsilon_3 \le A\arcsin\left(2\frac{\Delta_\alpha}{\sin\alpha}\right)\max\left\{\frac{\partial G}{\partial\theta}\right\}. \quad (16)$$

The deviation from the asymptote due to ε_3 is thus of the order of $\Delta_\alpha/\sin\alpha$ and may increase close to the antipode, if waves from a wide range of directions can reach that point. In practice this does not happen since continents and island chains block most of the arrival directions at the antipode, leaving only a small window of possible arrival directions [e.g. *Munk et al.*, 1963]. Directional wave spectra in active generation areas are generally relatively broad, $\partial G/\partial\theta/G$ is typically less than 2 for directions within 30° of the main wave direction. On the contrary, typical storm spectra can give $f\partial G/\partial f/G$ as large as 10 for frequencies within 30% of the peak frequency. We thus expect the deviation ε_2 to dominate over ε_3.

In order to use the asymptotic form $E_s \sim 1/(\alpha\sin\alpha)$, we first have to define its range of applicability, which is expected to depend on the spectral width of G, in both frequency and direction, in the source region, and the dimensions of the storm in the observation and transversal directions.

3.3. Verification of asymptotic swell height evolution

For a useful comparison with observations, the asymptotic swell height evolution should be approached on a scale smaller than the ocean basin scale. This is easily tested for storms with spatially uniform spectra over a radius r, by evaluating the integral in eq. (10). We chose a center frequency f_0 and consider the swell energy at a distance $R\alpha + \Delta_x$ and a time $t(\alpha)$ such that $R\alpha = gt/(4\pi f_0)$. Δ_x is thus an error relative to the theoretical position of the wave group of frequency f_0. The relative difference of $E_s(\alpha)$ and its asymptotic evolution $1/(\alpha\sin\alpha)$ depends only on the spectral shape in the storm, the relative frequency f_0/f_p where f_p is the peak frequency, the distance α, the storm size $\alpha/(r/R)$, and the position error Δ_x. Results are shown in figure 9 for isotropic directional spectra, in which case $\varepsilon_3 = 0$.

As indicated by eq. (15), the contribution of both the spectral shape and f_0/f_p comes through the maximum relative variation of F in the frequency interval that contribute to E_s. Here we take the spectra in the storm to have a JONSWAP shape [*Hasselmann et al.*, 1973], that we adjust

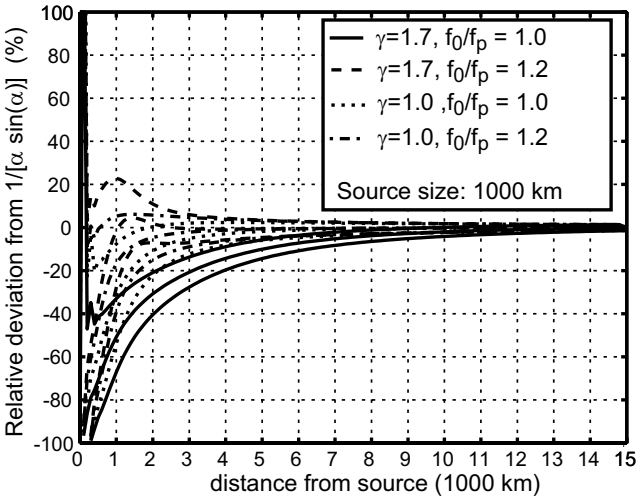

Figure 9. Convergence of the swell energy E_s integral (8) towards the asymptote $1/(\alpha\sin\alpha)$, as a function of spectrum width for a storm diameter of 1000 km. The result is independent of the choice of f_p. In practice the calculations were made for $f_p = 0.07$ Hz ($T_p = 13$ s). The three lines for each case correspond to position errors Δ_x of -200, 0 and 200 km relative to the great circle trajectory. For all cases considered here the deviation is less than 20% beyond 4000 km from the storm center.

by varying the peak enhancement factor γ. A relatively broad *Pierson and Moskowitz* [1964] spectrum is obtained with $\gamma = 1$. If we chose $f_0 = f_p$, this spectrum will give smaller deviations of E_s from the asymptote (solid lines in figure 9), than narrower spectra with larger values of γ. *Young* [2005] showed that wave spectra in Hurricanes generally fall in between these two categories, with a typical value $\gamma_J = 1.7$. Larger deviations from the asymptote are obtained for $f_0 < f_p$, since the forward face of the spectrum is very steep, while smaller errors are obtained for $f_0 > f_p$ due to the more gentle decrease of F towards the high frequencies.

Similarly, large deviations are produced if the observations are made in a direction far from the peak generation direction in cases when the directional spectrum is narrow. For observation directions 30° from the peak direction, and spectra with a cos^4 directional distribution, the deviations are still dominated by the dispersive term ε_2, as expected.

The other important factor is the distance α relative to the storm size $\varphi_{\max} = r/R$. A faster convergence is obtained for smaller storms. If observations do not correspond exactly to a theoretical propagation at a group speed C_g but are within a distance Δ_x of the theoretical position, the values of E_s will also be affected in a way that depends on the spectral shape. In the absence of energy gains or losses, and for realistic storm sizes and spectral shapes, the deviation of observations from the asymptote should be less than 20% for $x > 4000$ km when $\Delta_x < 200$ km is enforced.

These expected departures from the asymptotic evolution should be compared to those due to swell dissipation or generation. Even with perfect SAR observations, this is the intrinsic limit of the present method. A 20% error in energy conserving conditions may be misinterpreted as a dissipation or generation with an e-folding scale of the order of 20000 km, which gives a 20% energy change as waves propagate from 4000 to 8000 km away from the storm source.

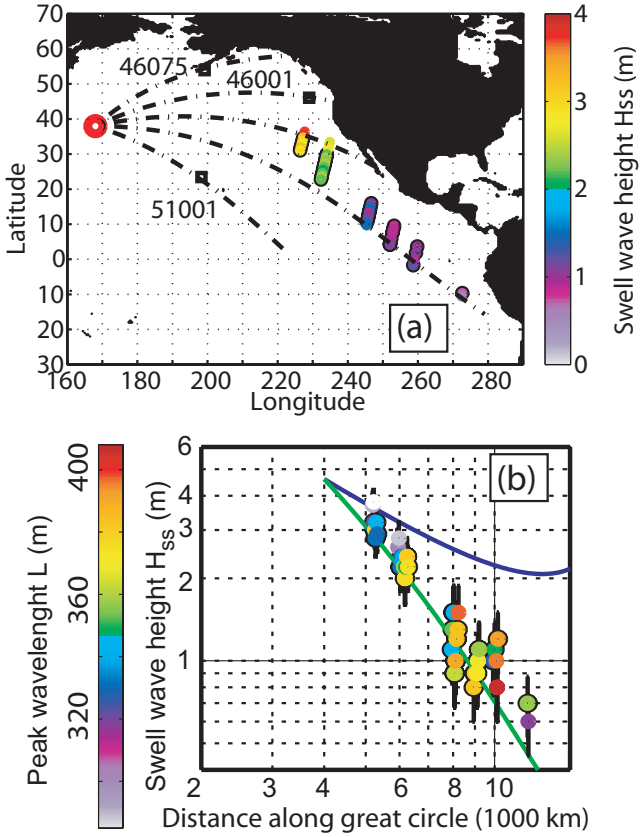

Figure 10. (a) Location of SAR observations with a 15 s peak period swell system corresponding to the 12 February source, with outgoing directions of 74 to 90°. The same swell was also observed at all buoys from 46075 off Western Alaska, to 51001 in Hawaii. The dash-dotted line represent great circles leaving the storm source with directions 42, 59, 74, 90 and 106°. (b) Observed swell wave height as a function of distance. The solid lines represent theoretical decays using no dissipation (blue), or a the fitted linear dissipation (green), for swells observed in February 2007. Circled dots are the observations used in the fitting procedure. Error bars show one standard deviation of the expected error on each SAR measurement.

3.4. Illustration

To illustrate the method described above, we analyse of one of the most powerful storms recorded over the past 4 years by ENVISAT's ASAR. Because the storm illustrated in figure 4 is not well suited due to the islands in the south-north swell tracks and the poor sampling of ENVISAT for the tracks going north-east from the storm, we have chosen the source found on February 12 2007 at 18:00 UTC, and located at 168 E and 38 N.

Using SAR-measured wave periods and directions at different times and locations, we follow great circle trajectories backwards at the theoretical group velocity. The location and date of the swell source is defined as the spatial and temporal center of the convergence area and time of the trajectories.

We chose a central peak period, here 15 s, and track the swells forward in space and time, starting from the source center at an angle θ_0, following ideal geodesic paths in search of SAR observations. Along each track, SAR data are selected if they are acquired within 3 hours and 100 km from the theoretical time and position. Great circle tracks are traced from the source in all directions, except for angular sectors with islands.

In order to obtain enough SAR data, we repeat this operation for regularly spaced values of θ_0 with a step of 2°. In our case, when varying θ_0 from 74 to 90° (counted clockwise from North), this procedure produced 58 SAR measurements with one swell partition that had a peak wavelength and direction within 50 m and 20° of the expected theoretical value.

If no energy is lost by the wave field, E_s decreases asymptotically as $1/[\alpha \sin(\alpha)]$ away from the source. Among the 58 swell observations, we further removed all the data within 4000 km of the source center, to make sure that the remaining data are in the far field of the storm, and data with a significant swell height H_{ss} less than 0.5 m, after bias correction based on the error model. This makes sure that the signal to noise ratio in the image is large enough so that the wave height estimation is accurate enough.

We then have 35 observations for which we assume that E_s is only a function of α, and we define the dissipation rate

$$\mu = -\frac{1}{E_s R}\frac{\mathrm{d}\,(E_s \alpha \sin\alpha)}{\mathrm{d}\alpha}. \qquad (17)$$

Positive values of μ correspond to losses of wave energy (figure 10). We then fit an analytical function $H_{ss}(\alpha)$ to the data, defined by a constant μ and $H_{ss}(\alpha = \pi/5)$, i.e. the swell height at 4000 km from the source. Here the couple $H_{ss}(\alpha = \pi/5) = 4.4$ m and $\mu = 3.7 \times 10^{-7}$ m^{-1} gives the least square difference between the decay with constant μ and the observed swell decays. Further, the uncertainty of that dissipation rate may be estimated from the known uncertainty of the SAR measurement of H_s, given by eq. (3)-(4). A more simple error model, with larger errors based

on the H_{s12} analysis by *Johnsen et al.* [2006], does not significantly alter this analysis. Using that error model and neglecting other sources of error in the present analysis, we perturbed the observed swell heights independently to produce a 400 ensemble of synthetic data sets. Taking the 16% and 84% levels in the estimation of μ, that would correspond to one standard deviation for a Gaussian distribution, we find that $3.1 \times 10^{-7} < \mu < 4.0 \times 10^{-7}$ at the 68% confidence level. This is the first ever estimation of the uncertainty on an observed swell dissipation rate. These values of μ are more than twice larger than reported by *Snodgrass et al.* [1966] for smaller amplitude swells.

The formidable height of 4.4 m at a distance of 4000 km was observed by the SAR for all outgoing directions from at least 74 to 106°. This same swell was also recorded by buoys in the North-East of Hawaii (NDBC buoy 51001), also with a peak period of 15 s, and a height of 3.4 m on 16 February 2007 at 0:00 UTC. That buoy is located 3300 km away from the center and in a direction close to 112°. Looking in the North-East quadrant of the storm, one also finds a trace of the swell at buoy 46005, off the Washington coast (4900 km in direction 59°). There the swell was also observed with a 15 s period and a maximum height of 3.2 m on February 17 at 17:00 UTC, similar to the SAR observations for the same distance. For directions closer to Northbound, either the generation was weaker or the Alaskan islands sheltered the coastal buoys. For example, the same swell was also recorded by NDBC buoy number 46075, off Shumagin Island, Alaska, at a distance of 3000 km from the source, in the direction 42°. At that buoy, the peak period was 15.0 s with a maximum swell height of 1.3 m on 15 February 2008 at 18:30 UTC.

Thus the power radiated by the storm is of the order of is 0.5 TW at 4000 km from the storm center, spread over a 50° angular sector. This power is about 16% of the estimated 3.2 TW annual mean flux that reaches the world's coastlines [*Rascle et al.*, 2008]. However, the observed dissipation rate corresponds to an e-folding scale of 3300 km for the energy. Taking an average propagation distance of 8000 km, only 160 GW would make it to the shore. If the same dissipation rate prevailed closer to the source, then the power radiated at 1000 km form the storm center was 1.4 TW.

We thus expect that the far field dissipation of swells, in spite of the small steepness of these swells, plays a significant role in the air-sea energy balance. This effect probably explains the systematic positive bias for predicted wave heights in wave models that neither account for swell dissipation nor assimilate wave measurements [see e.g. *Rascle et al.*, 2008].

4. Conclusions

Taking advantages of the satellite observations of unprecedented coverage and quality, investigations can repeat and complement the pioneering analysis of swell evolution performed in the 1960s. Severe storms can generate relatively broad spectra of large surface waves. But rapidly, the redistribution of energy, through linear dispersion and nonlinear interaction mechanisms, becomes very effective. The initial wind waves become swells outrunning the wind, leading to the apparition of coherent and quasi-deterministic persistent long-crested systems. The propagation properties of these surface gravity waves have been found to closely follow principles of geometrical optics. The coherent patterns of swell fronts dispersing over thousands of kilometers was shown to be useful to provide time series at "virtual buoys", filling gaps in space and time in between the orbit cycles of observation. Compared to buoy measurements, the present results correspond to an explicit dynamical validation of the SAR-derived spectral parameters. As the speed of waves in deep water is proportional to their period or wavelength, information carried by the SAR-derived period and direction distributions, observed at a fairly large distance from the generating area, pertains to the wind conditions existent up to 15 days before.

We also discussed how the swell energy should, in the absence of dissipation, decay in the far field of the storm like $1/(\alpha \sin \alpha)$ where α is the spherical distance between the storm center and observation point. Exploiting that property allowed us to estimate a dissipation rate μ of swell energy with unprecedented accuracy, establishing that swell dissipation can be a significant term in the global wave energy budget.

The proposed methodolgy performed here requires data far enough from the source, typically more than 4000 km, in order to approach this simple asymptotic behavior. At the same time, the swell amplitude should be large enough to be accurately measured by the SAR. Some knowledge of the spectral shape and its spatial distribution inside the storm may be useful to provide better estimates of μ for low dissipation cases, or closer to the storm centers. These further analyses will likely benefit from the joint use of data from altimeters, SARs, and other sources of spectral wave information.

A more systematic analysis and interpretation of this dissipation will be reported elsewhere [*Ardhuin et al.*, 2008a], with applications to wave forecasting models [*Ardhuin et al.*, 2008b, c]. The parameterization of the dissipation rate could also be used to produce a data-based forecasting system, extending our virtual buoy technique to the estimation of swell heights, with a forward propagation of observations.

Going in the opposite direction, toward the storm source, it is possible that the analysis of swell field could provide a "new" way of looking into the poorly observed structure of severe storms. Because the usual remote sensing techniques for estimating wind fields either do not work for very high winds or are not well validated [e.g. *Quilfen et al.*, 2006, 2007], the use of far-field swell information may provide an interesting complement to the local wind speeds and wave heights. This idea is not so "new", as [*Munk et al.*, 1963] already proposed an elegant heterodyning technique to push the spatial resolution for the estimation of storm location from swell data, while *Heimbach and Hasselmann* [2000] have proposed to use wave models to correct wind field errors. The quality of the SAR-derived swell parameters that are coming out of today's ENVISAT and tomorrow's Sentinel-1, together with a good understanding of the swell energy budget, including its dissipation revealed here, may finally enable this vision.

Acknowledgments. SAR data was provided by the European Space Agency (ESA) and buoy data was kindly provided by the U.S. National Data Buoy Center, and Marine Environmental Data Service of Canada. ESA funded the XCOL co-located database and the initial work on the virtual buoy concept. The swell decay analysis was funded by the French Navy as part of the EPEL program. This work is a contribution to the ANR-funded project HEXECO and DGA-funded project ECORS.

References

Alpers, W. R., and C. L. Rufenach (1981), The effect of orbital motions on synthetic aperture radar imagery of ocean waves, *IEEE Trans. Antennas Propagat.*, *27*(C7), 685–690.

Aouf, L., J.-M. Lefèvre, D. Hauser, and B. Chapron (2006), On the combined assimilation of RA-2 altimeter and ASAR wave data for the improvement of wave forcasting, in *Proceedings of 15 Years of Radar Altimetry Symposium, Venice, March 13-18*.

Ardhuin, F., B. Chapron, and F. Collard (2008a), Strong decay of steep swells observed across oceans, *Geophys. Res. Lett.*, *submitted*.

Ardhuin, F., F. Collard, B. Chapron, P. Queffeulou, J.-F. Filipot, and M. Hamon (2008b), Spectral wave dissipation based on observations: a global validation, in *Proceedings of Chinese-German Joint Symposium on Hydraulics and Ocean Engineering, Darmstadt, Germany*.

Ardhuin, F., L. Marié, N. Rascle, P. Forget, and A. Roland (2008c), Observation and estimation of Lagrangian, Stokes and Eulerian currents induced by wind and waves at the sea surface, *J. Phys. Oceanogr.*, submitted, available at http://hal.archives-ouvertes.fr/hal-00331675/fr/.

Breivik, L. A., M. Reistad, H. Schyberg, J. Sunde, H. E. Krogstad, and H. Johnsen (1998), Assimilation of ERS SAR wave spectra in an operational wave model, *J. Geophys. Res.*, *103*, 7887–7900.

Chapron, B., H. Johnsen, and R. Garello (2001), Wave and wind retrieval from SAR images of the ocean, *Ann. Telecommun.*, *56*, 682–699.

Collard, F., F. Ardhuin, and B. Chapron (2005), Extraction of coastal ocean wave fields from SAR images, *IEEE J. Oceanic Eng.*, *30*(3), 526–533.

Collard, F., B. Chapron, F. Ardhuin, H. Johnsen, and G. Engen (2006), Coastal ocean wave retrieval from ASAR complex images, in *Proceedings of OceanSAR*, Earth Observation Marine Surveillance Coordination Comittee, Saint John's, Canada.

Darbyshire, J. (1958), The generation of waves by wind, *Phil. Trans. Roy. Soc. London A*, *215*(1122), 299–428.

Dore, B. D. (1978), Some effects of the air-water interface on gravity waves, *Geophys. Astrophys. Fluid. Dyn.*, *10*, 215–230.

Engen, G., and H. Johnsen (1995), Sar-ocean wave inversion using image cross spectra, *IEEE Trans. on Geosci. and Remote Sensing*, *33*, 4.

Gerling, T. W. (1992), Partitioning sequences and arrays of directional ocean wave spectra into component wave systems, *J. Atmos. Ocean Technol.*, *9*, 444–458.

Gjevik, B., H. E. Korgstad, A. Lygre, and O. Rygg (1988), long period swell wave events on the Norwegian shelf, *J. Phys. Oceanogr.*, *18*, 724–737.

Grachev, A. A., and C. W. Fairall (2001), Upward momentum transfer in the marine boundary layer, *J. Phys. Oceanogr.*, *31*, 1698–1711.

Hanson, J. L., and O. M. Phillips (2001), Automated analysis of ocean surface directional wave spectra, *J. Atmos. Ocean Technol.*, *18*, 277–293.

Hasselmann, K., et al. (1973), Measurements of wind-wave growth and swell decay during the Joint North Sea Wave Project, *Deut. Hydrogr. Z.*, *8*(12), 1–95, suppl. A.

Hasselmann, S., C. Brüning, and K. Hasselmann (1996), An improved algorithm for the retrieval of ocean wave spectra from synthetic aperture radar image spectra, *J. Geophys. Res.*, *101*, 16,615–16,629.

Hasselmann, S., P. Lionello, and K. Hasselmann (1997), An optimal interpolation scheme for the assimilation of spectral wave data, *J. Geophys. Res.*, *102*, 15,823–15,836.

Heimbach, P., and K. Hasselmann (2000), Development and application of satellite retrievals of ocean wave spectra, in *Satellites, oceanography and society*, edited by D. Halpern, pp. 5–33, Elsevier, Amsterdam.

Holt, B., A. K. Liu, D. W. Wang, A. Gnanadesikan, and H. S. Chen (1998), Tracking storm-generated waves in the northeast pacific ocean with ERS-1 synthetic aperture radar imagery and buoys, *J. Geophys. Res.*, *103*(C4), 7917–7929.

Johnsen, H., and F. Collard (2004), ASAR wave mode processing - validation of reprocessing upgrade. technical report for ESA-ESRIN under contract 17376/03/I-OL, *Tech. Rep. 168*, NORUT.

Johnsen, H., G. Engen, F. Collard, V. Kerbaol, and B. Chapron (2006), Envisat ASAR wave mode products - quality assessment and algorithm upgrade, in *Proceedings of SEASAR 2006, SP-613*, ESA, ESA - ESRIN, Frascati, Italy.

Kedar, S., M. Longuet-Higgins, F. W. N. Graham, R. Clayton, and C. Jones (2008), The origin of deep ocean microseisms in the north Atlantic ocean, *Proc. Roy. Soc. Lond. A*, pp. 1–35, doi:10.1098/rspa.2007.0277.

Kerbaol, V., B. Chapron, and P. Vachon (1998), Analysis of ERS-1/2 synthetic aperture radar wave mode imagettes, *J. Geophys. Res.*, *103*(C4), 7833–7846.

Krogstad, H. E. (1992), A simple derivation of Hasselmann's nonlinear ocean-synthetic aperture radar transform, *J. Geophys. Res.*, *97*(C2), 2421–2425.

Munk, W. H., G. R. Miller, F. E. Snodgrass, and N. F. Barber (1963), Directional recording of swell from distant storms, *Phil. Trans. Roy. Soc. London A*, *255*, 505–584.

Pierson, W. J., Jr, and L. Moskowitz (1964), A proposed spectral form for fully developed wind seas based on the similarity theory of S. A. Kitaigorodskii, *J. Geophys. Res.*, *69*(24), 5,181–5,190.

Quilfen, Y., J. Tournadre, and B. Chapron (2006), Altimeter dual-frequency observations of surface winds, waves, and rain rate in tropical cyclone isabel, *J. Geophys. Res.*, *87*(111), C01,004, doi:10.1029/2005JC003068.

Quilfen, Y., C. Prigent, B. Chapron, A. A. Mouche, and N. Houti (2007), The potential of quikscat and windsat observations for the estimation of sea surface wind vector under severe weather conditions, *J. Geophys. Res.*, *112*, C09,023, doi:10.1029/2007JC004163.

Rascle, N., F. Ardhuin, P. Queffeulou, and D. Croizé-Fillon (2008), A global wave parameter database for geophysical applications. part 1: wave-current-turbulence interaction parameters for the open ocean based on traditional parameterizations, *Ocean Modelling*, *25*, 154–171, doi:10.1016/j.ocemod.2008.07.006.

Schulz-Stellenfleth, J., S. Lehner, and D. Hoja (2005), A parametric scheme for the retrieval of two-dimensional ocean wave spectra from synthetic aperture radar look cross spectra, *J. Geophys. Res.*, *110*, C05,004, doi:10.1029/2004JC002822.

Snodgrass, F. E., G. W. Groves, K. Hasselmann, G. R. Miller, W. H. Munk, and W. H. Powers (1966), Propagation of ocean swell across the Pacific, *Phil. Trans. Roy. Soc. London*, *A249*, 431–497.

WISE Group (2007), Wave modelling the state of the art, *Progress in Oceanography*, *75*, 603–674, doi:10.1016/j.pocean.2007.05.005.

Young, I. R. (2005), Directional spectra of hurricane wind waves, *J. Geophys. Res.*, *111*, C08,020, doi:10.1029/2006JC003540.

Fabrice Collard, Collecte Localisation Satellites, division Radar, 29280 Plouzané, France. (Dr.fab@cls.fr)

Fabrice Ardhuin, Service Hydrographique et Océanographique de la Marine, 29609 Brest, France. (ardhuin@shom.fr)

Bertrand Chapron, Ifremer, Laboratoire d'Océanographie Spatiale, Centre de Brest, 29280 Plouzané, France. (bertrand.chapron@ifremer.